Nano-second temporal particle behavior in high-power impulse magnetron sputtering discharge in a cylindrical cathode (EP)

Suihan Cui, Zhongzhen Wu (iD), Shu Xiao, Bocong Zheng, Lei Chen, Tijun Li, Ricky K. Y. Fu, Paul K. Chu (iD), Xiubo Tian, Wenchang Tan, Daining Fang, and Feng Pan

COLLECTIONS

(EP) This paper was selected as an Editor's Pick

View Online   Export Citation   CrossMark

ARTICLES YOU MAY BE INTERESTED IN

Spin-split valence bands of the ferromagnetic insulator $Cr_2Ge_2Te_6$ studied by angle-resolved photoemission spectroscopy
Journal of Applied Physics **127**, 023901 (2020); https://doi.org/10.1063/1.5135759

Hollow cathode effect modified time-dependent global model and high-power impulse magnetron sputtering discharge and transport in cylindrical cathode
Journal of Applied Physics **125**, 063302 (2019); https://doi.org/10.1063/1.5048554

Spatially resolved light field analysis of the second-harmonic signal of $\chi^{(2)}$-materials in the tight focusing regime
Journal of Applied Physics **127**, 023103 (2020); https://doi.org/10.1063/1.5133476

Nano-second temporal particle behavior in high-power impulse magnetron sputtering discharge in a cylindrical cathode

Suihan Cui,[1,2] Zhongzhen Wu,[1,a)] Shu Xiao,[1,3] Bocong Zheng,[1] Lei Chen,[1] Tijun Li,[1] Ricky K. Y. Fu,[3] Paul K. Chu,[3] Xiubo Tian,[1] Wenchang Tan,[1] Daining Fang,[2] and Feng Pan[1]

AFFILIATIONS

[1]School of Advanced Materials, Peking University Shenzhen Graduate School, Shenzhen 518055, China
[2]College of Engineering, Peking University, Beijing 100871, China
[3]Department of Physics and Materials Science, City University of Hong Kong, Tat Chee Avenue, Kowloon, Hong Kong 999077, China

[a)]Author to whom correspondence should be addressed: wuzz@pkusz.edu.cn. Tel./Fax: +86-755-26032957.

ABSTRACT

Systematic analysis of discharge processes is needed for a good understanding of the physical mechanism that enables optimal coating deposition, especially pulsed discharges sustained by high voltages and large currents. Owing to the temporal and complex characteristics of the discharge process and relatively simplistic analytical methods, the discharge process and particle evolution in high-power impulse magnetron sputtering (HiPIMS) are still not well understood. In this work, a cylindrical cathode is introduced to restrict the discharge and delay plasma loss, and a global model is established to simulate the discharge on a Cr target in N_2/Ar. Particles with different reaction energies appearing successively produce an asynchronous discharge phenomenon, and a series of inflection points corresponding to different physical processes including excitation, sputtering, ionization, and diffusion are observed from the particle density evolution curves. High-precision and time-resolved spectrometry (400 ns) is utilized to monitor the evolution of particles with time, and inflection points predicted by the model are observed experimentally to verify the particle behavior in the HiPIMS discharge.

Published under license by AIP Publishing. https://doi.org/10.1063/1.5127565

I. INTRODUCTION

High-power impulse magnetron sputtering (HiPIMS)[1–3] is a physical vapor deposition (PVD) technique in which high-density plasmas are produced by applying high-power pulses to the magnetron target.[4] The high metal ionization rate[4,5] improves the ion energy controllability[6,7] and coating properties.[8–11] However, owing to the high voltage and large current in the discharge pulse, the HiPIMS discharge process is quite complex, and the plasma composition, energy, and electron temperature vary with the pulse time.

Investigation of the evolution of discharge by means of the current with time relationship is a common experimental method to analyze the HiPIMS discharge process.[12–14] In the HiPIMS discharge pulses, the target current exhibits an obvious peak and then turns into a platform indicating two different discharge stages.[12] By studying the effects of the discharge pressure[15] and materials[12,16] on the target current shape, the target current peak is found to be mainly caused by the avalanche effect in conjunction with sputtering and gas rarefaction effects. Anders[7] found that target materials with high sputtering yield (Cu) could be operated in a sustained gasless mode based on the target current study. Čapek et al.[17] realized high-intensity discharge and performed a rapid deposition of low sputtering yield materials by controlling the shape of the target current peak and platform by magnetic fields. However, the target current depends on the combined effects of electron emission, ion sputtering, Hall current, and other factors,[13] and the behavior of a single ion or neutral particle cannot be determined accurately. Therefore, studies based on the target current do not provide a clear understanding of the HiPIMS discharge. Optical emission spectroscopy (OES) has been employed to track and measure the evolution of different species in the plasma in HiPIMS discharge and found that the discharge intensity and metal ionization rate increase with discharge power.[18,19] Large amounts of bivalent ions or even polyvalent ions are produced in the high-density plasma,[20]

but as a result of the relatively poor time resolution of OES ($>10\,\mu s$) and rapid evolution, especially in the initial stage of HiPIMS discharge, it is difficult for OES to describe the details of the evolution of each particle in the plasma and its influence on the discharge process. Although some new techniques such as terahertz time domain spectroscopy (TDS)[21] and incoherent Thomson scattering[22] were developed recently to significantly lower the time resolution, many limitations in plasma diagnosis still exist. In view of the experimental shortcomings, a theoretical simulation based on the global model[23–25] has been proposed. Gudmundsson[26] studied the HiPIMS discharge process with the time-dependent global model and found that electron impact ionization and charge exchange were dominant in the generation of metal ions during and after the initial pulse, respectively. An ionized region was introduced into the global model to calculate the ionization rate of different target materials,[27] and the effects of the discharge parameters on the plasma were studied by incorporating the composite targets and target poisoning characteristics into the model.[28] However, since the global model is based on some assumptions

and simplification, the simulation results lack experimental verification, and some details about the particle behaviors are ignored.

In this work, the discharge process of HiPIMS in the popular system (Ar/N$_2$/Cr)[29] is analyzed systematically by theoretical simulation and experiments. The density evolution curves of the typical particles in the system are calculated, showing an asynchronous discharge phenomenon and a series of inflection points that determine all the physical processes. At last, time-resolved optical emission spectroscopy is used to confirm the simulations and the interactions of each physical process.

II. SIMULATION AND EXPERIMENTS

To reduce the plasma diffusion loss, a cylindrical cathode[30] made of chromium (99.9%) with an inner diameter of 120 mm and a width of 48 mm is adopted to limit the discharge as shown in Fig. 1(a). Two cylindrical magnets are placed on the periphery of the target, and since the plasma discharge occurs inside the cylindrical cathode, the hollow cathode effect[31] is introduced to modify
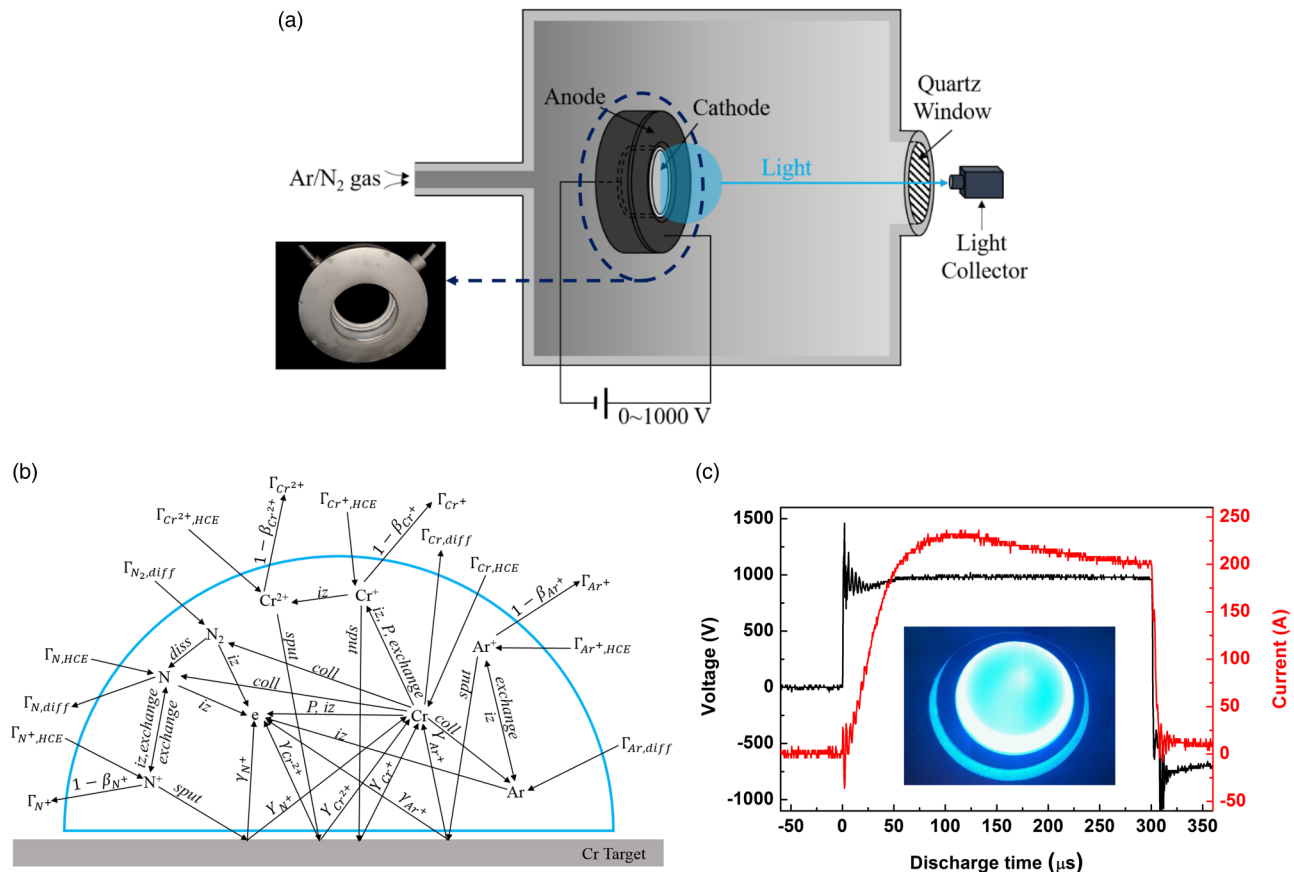
FIG. 1. (a) Schematic of the vacuum device. (b) Schematic illustration of the global model modified by the hollow cathode effect showing the balance and reactions of the main particles in the ionization region. The subscripts are defined as follows: chexc, charge exchange; coll, collision; diff, diffusion; diss, dissociation; iz, ionization; P, Penning ionization; sput, sputtering; and HCE, hollow cathode effect. (c) Current and voltage signal in a pulse at 1000 V and 1.5 Pa together with a picture showing the glow in the cylindrical cathode.

the time-dependent global model[30] (see the Appendix) as shown in Fig. 1(b) (simplified from Fig. 7). According to the density balance equations of the particles such as cold electrons (e), hot electrons (e^H), ground state neutral particles (Ar, N_2, N, and Cr), energetic atoms (Ar^H), metastable neutral particles (Ar^m and N_2^m), singly charged ions (Ar^+, N_2^+, N^+, and Cr^+), doubly charged ions (Cr^{2+}), and the electron energy balance equation, the particle density and electron energy in the discharge zone can be simulated according to the discharge time, and detailed particle evolution in the discharge can be characterized. The inputs to the model are the current and voltage waveforms obtained experimentally from the HiPIMS discharge in a vacuum chamber[32,33] with dimensions of $600 \times 600 \times 500$ mm^3. Ar (99.99%, 10 SCCM) and N_2 (99.999%, 5 SCCM) are used, and the discharge pressure is 1.5 Pa. The discharge voltage is 1000 V, the pulse width is 300 μs, and the frequency is 50 Hz. The target voltage and current waveforms are obtained by an oscilloscope connected to the power supply, and the waveforms and HiPIMS image are shown in Fig. 1(c). An observation window is installed on the side of the vacuum chamber opposite to the cathode outlet to collect spectral information via a spectrometer.

III. RESULTS AND DISCUSSIONS

The density curves of each particle in the Ar/N_2/Cr HiPIMS system vs discharge time is obtained by the global model as shown in Figs. 2(a)–2(c), and only the data in the first 100 μs of the whole pulse are shown for comparison. The simulation results of the whole pulse calculated by global model is shown in Fig. 8. All the particles in the plasma are generated after discharge ignition except Ar and N_2, which are the original working gases. After the pulse voltage initiates, the electrons collide with atoms and molecules in the working gas to ignite the discharge. The main reactions in the global model are shown in Table I. In the plasma, Ar exists in the form of Ar, Ar^+, Ar^m, and Ar^H. In the beginning of the discharge, ionization collisions (reaction 1) and excitation collisions (reaction 2) take place between electrons and Ar atoms, and consequently, Ar^+ and Ar^m are generated resulting in a gradual decrease of Ar and rapid increase of Ar^+ and Ar^m. Ar^m is unstable because of easy de-excitation (reaction 3) and further ionization (reaction 4), and, therefore, the peak density of Ar^m is about an order of magnitude less than that of Ar^+. The evolution of Ar^H follows closely that of Ar^+ because Ar^H is generated by recombination when Ar^+ sputters the target.[34] With the accumulation of Ar in the ionization region, significant diffusion begins after 25 μs and the particle densities start to decline. Meanwhile, high-density Cr atoms generated by sputtering collide with the gas particles to accelerate the process.[14] After 100 μs, the particle density reaches an equilibrium.

The initial form of nitrogen is N_2, which is ionized (reaction 5), excited (reaction 6), and dissociated (reaction 8), due to collisions with electrons to generate N_2^+, N_2^m, and N, respectively. Therefore, with the gradually decreasing N_2 density, N_2^+, N_2^m, and N increase almost simultaneously. In particular, the N_2^+ density is significantly less than those of the other two species and decays faster because N_2 ionization (reaction 5) needs a higher electron temperature and N_2^m is preferentially de-excited (reaction 11) rather than ionized (reaction 7). Sputtering and further dissociation occur for N_2^+ (reaction 9) resulting in a loss. N^+ is generated after N is

produced and ionized and so N^+ appears at last with the smallest density. Since the N_2^+ and N^+ densities are one or two orders of magnitude smaller than that of Ar^+, it can be inferred that sputtering in the gas discharge results from Ar^+ bombardment. After
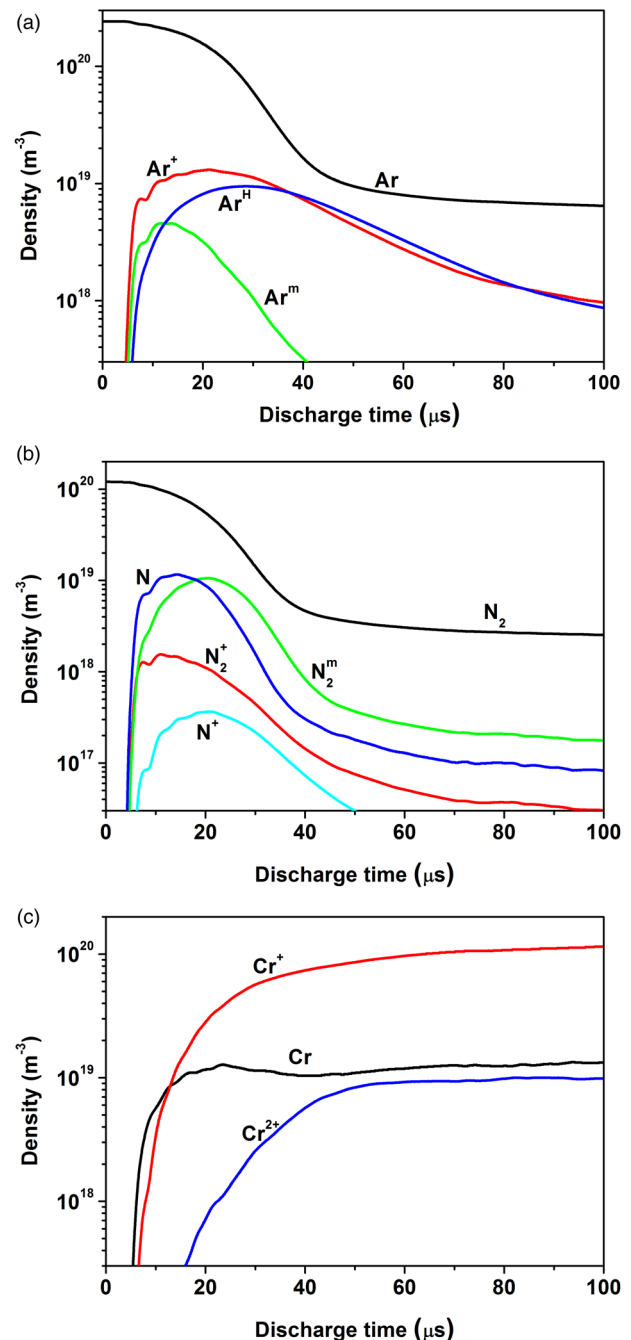

FIG. 2. Density evolution curves with time: (a) Ar, (b) N, and (c) Cr in the initial 100 μs of the HiPIMS pulse.

TABLE I. Main reactions in the Ar/N$_2$/Cr plasma.

No.	Reaction	Threshold (eV)	Reference
1	$e + Ar \rightarrow Ar^+ + 2e$	15.76	35
2	$e + Ar \rightarrow Ar^m + e$	11.56	35
3	$e + Ar^m \rightarrow Ar + e$	−11.56	35
4	$e + Ar^m \rightarrow Ar^+ + 2e$	4.2	35
5	$e + N_2 \rightarrow N_2^+ + 2e$	15.6	36
6	$e + N_2 \rightarrow N_2^m + e$	6.17	36
7	$e + N_2^m \rightarrow N_2^+ + 2e$		37
8	$e + N_2 \rightarrow 2N + e$	9.76	38
9	$e + N_2^+ \rightarrow 2N$		39
10	$e + N \rightarrow N^+ + 2e$	14.54	36
11	$N_2^m \rightarrow N_2 + h\nu$		36
12	$e + Cr \rightarrow Cr^+ + 2e$	6.8	40
13	$e + Cr^+ \rightarrow Cr^{2+} + 2e$	15.0	40
14	$Ar^+ + Cr^+ \rightarrow Cr^+ + Ar$		

$20\,\mu$s, the N particles decline rapidly due to the diffusion and collision because of the smaller mass than Ar.

The generation of Cr particles (Cr, Cr$^+$, and Cr^{2+}) in the plasma is quite different from that of the gas particles and shows a gradual increase with discharge time. Cr is produced by sputtering of Ar$^+$, N$_2^+$, and N$^+$ and then ionized by reaction 12 or charge exchange (reaction 14) to produce Cr$^+$. Cr^{2+} is produced by secondary ionization (reaction 13). Therefore, Cr, Cr$^+$, and Cr^{2+} are generated in sequence. In the discharge process, the density of metal ions increases and self-sputtering is enhanced. Therefore, the Cr particle density does not decrease significantly despite the decay of gas ions at $40\,\mu$s. After $60\,\mu$s, Cr particles reach an equilibrium and become the main discharge species in the system, indicating that the system enters the metal-dominant discharge stage from the gas-dominant discharge stage.
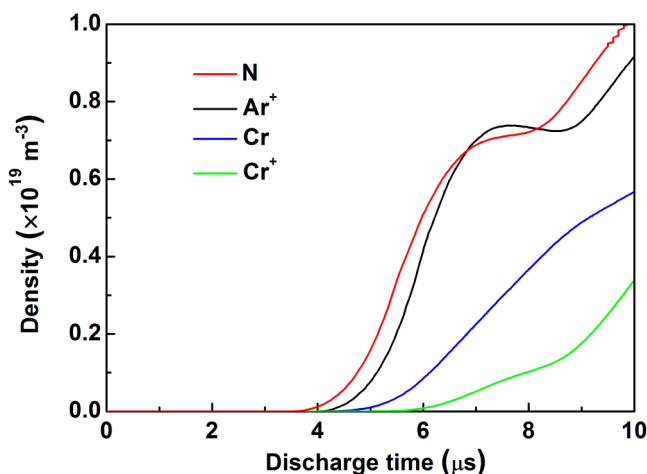

FIG. 3. Evolution curves of N, Ar$^+$, Cr, and Cr$^+$ in the first $10\,\mu$s of the HiPIMS pulse.

Four representative particles (N, Ar$^+$, Cr, and Cr$^+$) are selected, and the evolution curves in the first $10\,\mu$s are presented in Fig. 3. N, Ar$^+$, Cr, and Cr$^+$ increase in turn indicating an asynchronous discharge phenomenon. Generally, the glow discharge starts from gas discharge, but N is generated slightly earlier than Ar$^+$ because the dissociation energy (9.76 eV) of N$_2$ is smaller than the ionization energy (15.76 eV) of Ar atoms and, consequently, the dissociation reaction takes place more easily. Compared to gas particles, Cr atoms appear later and the density increases more slowly, resulting from the generation of Cr atoms, which mainly depends on Ar$^+$ sputtering. Cr$^+$ is produced by Cr ionization and charge exchange, and so the Cr$^+$ curve increases at last. In this initial stage of HiPIMS, the discharge sequence of gas particles depends on the reaction energy, whereas that of the metal particles depends on the sequence of the physical processes.

A series of inflection points can be found from the different particle curves with the discharge time. Here, five species (N, Ar$^+$, Cr, Cr$^+$, and Cr^{2+}) are taken as examples, and they correspond to five species in the plasma: gas atoms, gas ions, metal atoms, metal univalent ions, and bivalent metal ions, as shown in Figs. 4(a)–4(c). The particle equilibrium equation of N is shown in Eq. (1) [simplified from Eq. (A11)]. The five terms in the polynomial correspond to five physical processes, such as dissociation of N$_2$ and N$_2^+$, ionization, and diffusion and collision with Cr,

$$\frac{dn_N}{dt} = 2k_{diss,N_2} n_{N_2} n_e + 2k_{diss,N_2^+} n_{N_2} n_e - k_{iz,N} n_N n_e - \boldsymbol{\Gamma}_{N,diff} \frac{S_{IR} - S_T}{V_{IR}}$$
$$- \boldsymbol{\Gamma}_{Cr,coll} \frac{m_{Cr}}{m_N} \frac{n_N}{n_{gas}} \frac{S_{IR} - S_T}{V_{IR}}, \tag{1}$$

where n (1/m^3) is the density, k (m^3/s) is the rate coefficient, m (kg) is the particle mass, and $\boldsymbol{\Gamma}_{coll}$ [1/(m^2 s)] and $\boldsymbol{\Gamma}_{diff}$ [1/(m^2 s)] are the fluxes produced by collision of the "sputtering wind" and diffusion, respectively. S_T (m^2), S_{IR} (m^2), and V_{IR} (m^3) are the geometric parameters in the ionization region representing the contact area on the target, surrounding area, and volume, respectively. In the beginning of the discharge, N mainly exists in the form of N$_2$. Only the dissociation of N$_2$ and N$_2^+$ occurs and, therefore, the density of N increases rapidly. With increasing discharge, N is consumed by ionization and inflection point 1 occurs at $6\,\mu$s [Fig. 4(a)]. The discharge intensity continues to increase, and the dissociation reactions do not decline. Hence, the N density continues to increase rapidly after slight fluctuations. When the N density in the ionization region reaches a certain value, a concentration difference is formed resulting in outward diffusion from the ionization region. The N density reaches the maximum at inflection point 2 when diffusion is equal to the generation at $20\,\mu$s. Meanwhile, large amounts of Cr atoms are produced in the ionization region upon collision with N atoms thereby accelerating N overflow and hindering the replenishment of external N$_2$ by collision giving rise to a rapid decline in the N density curve. Production and consumption of N atoms reach an equilibrium at $30\,\mu$s, and the N density curve does not change anymore.

The particle equilibrium equation of Ar$^+$ includes mainly neutrals (Ar, Ar^m, and Ar^H) ionization, sputtering, outward diffusion, and charge exchange as shown in Eq. (2) [simplified from Eq. (A4)],
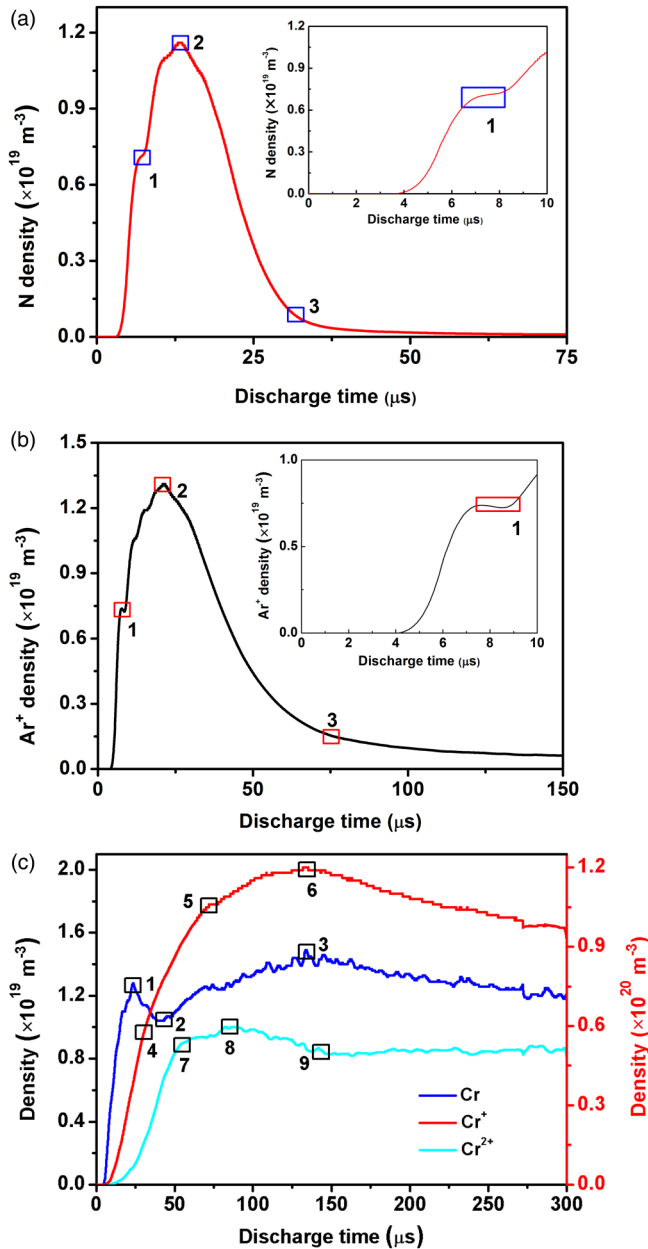
FIG. 4. Density curves of (a) N, (b) Ar$^+$, and (c) Cr, Cr$^+$, and Cr^{2+} vs discharge time.

$$\frac{dn_{\mathrm{Ar}^+}}{dt} = k_{\mathrm{iz}}n_{\mathrm{Ar}}n_{\mathrm{e}} + k_{\mathrm{iz}}n_{\mathrm{Ar}^{\mathrm{H}}}n_{\mathrm{e}} + k_{\mathrm{miz}}n_{\mathrm{Ar}^{\mathrm{m}}}n_{\mathrm{e}} - \boldsymbol{\Gamma}_{\mathrm{Ar}^+}\frac{S_{\mathrm{T}}}{V_{\mathrm{IR}}}$$
$$- \boldsymbol{\Gamma}_{\mathrm{Ar}^+}(1-\beta_{\mathrm{Ar}^+})\frac{S_{\mathrm{IR}}-S_{\mathrm{T}}}{V_{\mathrm{IR}}} - k_{\mathrm{chexc}}n_{\mathrm{Ar}^+}n_{\mathrm{Cr}}, \qquad (2)$$

where β is the ion return probability. Different from N, Ar$^+$ can be generated directly by electron collision with Ar, Ar$^{\mathrm{m}}$, and Ar$^{\mathrm{H}}$

because Ar is a monatomic gas. Hence, the Ar$^+$ density increases faster than N. Owing to the negative potential on the target, some of the Ar$^+$ ions move toward the target and disappear. However, as the discharge proceeds, the Ar$^+$ density fluctuates at $7\,\mu$s (inflection 1) and continues to increase as shown in Fig. 4(b). Similar to N, when the concentration of Ar$^+$ reaches a certain value, it starts to diffuse outward from the ionization region. Besides, with increasing Ar$^+$ density, sputtering and charge exchange with Cr become more prevalent. The Ar$^+$ density attains the maximum at inflection point 2 ($25\,\mu$s) after which consumption is greater than generation. With decreasing Ar$^+$ density, consumption continues to decrease, and, finally, the Ar$^+$ density reaches an equilibrium at $75\,\mu$s and inflection point 3 appears.

Compared to gas particles, the evolution of metal particles is more complex as shown in Fig. 4(c). Cr atoms are generated primarily by sputtering of Ar$^+$, Cr$^+$, and Cr^{2+} and consumed by charge exchange and diffusion. The particle balance equation is shown in Eq. (3) [simplified from Eq. (A13)],

$$\frac{dn_{\mathrm{Cr}}}{dt} = \boldsymbol{\Gamma}_{\mathrm{Ar}^+}Y_{\mathrm{Ar}^+}\frac{S_{\mathrm{T}}}{V_{\mathrm{IR}}} + \boldsymbol{\Gamma}_{\mathrm{Cr}^+}Y_{\mathrm{Cr}^+}\frac{S_{\mathrm{T}}}{V_{\mathrm{IR}}} + \boldsymbol{\Gamma}_{\mathrm{Cr}^{2+}}Y_{\mathrm{Cr}^{2+}}\frac{S_{\mathrm{T}}}{V_{\mathrm{IR}}}$$
$$- k_{\mathrm{iz,Cr}}n_{\mathrm{Cr}}n_{\mathrm{e}} - k_{\mathrm{chexc}}n_{\mathrm{Ar}^+}n_{\mathrm{Cr}} - \boldsymbol{\Gamma}_{\mathrm{Cr,diff}}\frac{S_{\mathrm{IR}}-S_{\mathrm{T}}}{V_{\mathrm{IR}}}, \qquad (3)$$

where Y is the sputtering yield calculated by TRIM.[41] In the initial stage of the discharge, Cr is generated by Ar$^+$ sputtering and increases rapidly with increasing Ar$^+$ density. Afterward, electron impact collisions produce substantial ionization of Cr and charge exchange starts to occur. With increasing plasma density, consumption of Cr surpasses generation resulting in the delay at $25\,\mu$s (inflection 1). When the Cr ion density (including Cr$^+$ and Cr^{2+}) is high, self-sputtering is enhanced[7,17] and becomes the primary sputtering mechanism instead of gas sputtering leading to a fast replenishment of Cr. Consequently, the Cr density reaches a minimum value at $50\,\mu$s (inflection 2), and after that, the Cr density curve increases again reaching the maximum at $140\,\mu$s and then decreases slowly due to diffusion.

The generation and consumption of Cr$^+$ are shown in Eq. (4) [simplified by Eq. (A15)]. The generation terms are ionization of Cr and charge exchange of Cr with Ar$^+$, and the loss terms are sputtering, diffusion, and secondary ionization,

$$\frac{dn_{\mathrm{Cr}^+}}{dt} = k_{\mathrm{iz,Cr}}n_{\mathrm{Cr}}n_{\mathrm{e}} + k_{\mathrm{chexc}}n_{\mathrm{Ar}^+}n_{\mathrm{Cr}} - \boldsymbol{\Gamma}_{\mathrm{Cr}^+}\frac{S_{\mathrm{T}}}{V_{\mathrm{IR}}}$$
$$- \boldsymbol{\Gamma}_{\mathrm{Cr}^+}(1-\beta_{\mathrm{Cr}^+})\frac{S_{\mathrm{IR}}-S_{\mathrm{T}}}{V_{\mathrm{IR}}} - k_{\mathrm{iz,Cr}^+}n_{\mathrm{Cr}^+}n_{\mathrm{e}}. \qquad (4)$$

Because the generation of Cr$^+$ depends on ionization of Cr, the inflection points of Cr$^+$ lags behind that of Cr. Two fluctuations can be observed at $30\,\mu$s (inflection 4) and $75\,\mu$s (inflection 5) from the Cr$^+$ density curve corresponding to Cr$^+$ sputtering and secondary ionization, respectively. Under an enhanced outward diffusion, the Cr$^+$ density decreases slowly after reaching the maximum value at $140\,\mu$s (inflection 6). It is noted that the Cr$^+$ density exceeds 10^{20} m^{-3} and Cr$^+$ becomes the species with the largest proportion

in the plasma after inflection 5, suggesting that the subsequent discharge is dominated by strong metal discharge and self-sputtering.

Cr^{2+} is produced by ionization of Cr^{+} and consumption is mainly due to sputtering and diffusion as shown in Eq. (5) [simplified from Eq. (A16)],

$$\frac{dn_{Cr^{2+}}}{dt} = k_{iz,Cr^{+}} n_{Cr^{+}} n_{e} - \boldsymbol{\Gamma}_{Cr^{2+}} \frac{S_{T}}{V_{IR}} - \boldsymbol{\Gamma}_{Cr^{2+}} (1 - \beta_{Cr^{2+}}) \frac{S_{IR} - S_{T}}{V_{IR}}. \quad (5)$$

Cr^{2+} generated after Cr^{+} and the fluctuation is due to the return to the target occurring at 50 μs (inflection 7). Different from Cr^{+}, Cr^{2+} is difficult to be further ionized to form polyvalent ions.[39] Inflection 8 is mainly caused by outward diffusion, and afterward, the Cr^{2+} density starts to decline and reaches an equilibrium at 140 μs (inflection 9).

The average electron temperature T_{e} (eV) verifies the evolution of each physical process in the ionization region, as shown in Fig. 5. In the initial stage of discharge, the temperature of electrons increases significantly due to the sudden rise in the voltage. At this time, electrons collide with the working gas (Ar and N_{2}) to excite or ionize the gas particles. Therefore, the HiPIMS discharge enters the gas-dominant discharge stage, and electron impact is the predominant discharge mechanism. As a result of electron impact, the electron temperature decreases rapidly and reaches a minimum of 2.5 eV at 20 μs (inflection 1). As the gas ion (Ar^{+}) density reaches the maximum, ionization collisions decline and high-energy secondary electrons are produced by gas ions sputtering[42] resulting in a slow increase in the electron temperature. When sputtering renders metal atoms the main species in the plasma, the HiPIMS discharge enters the metal-dominant discharge stage. At this time, sputtering is dominated by Cr^{+} self-sputtering that hardly generates secondary electrons.[43] Besides, ionization of Cr, especially secondary ionization of Cr^{+}, requires a higher electron temperature, and, therefore, the electron temperature curve exhibits inflection 2 at
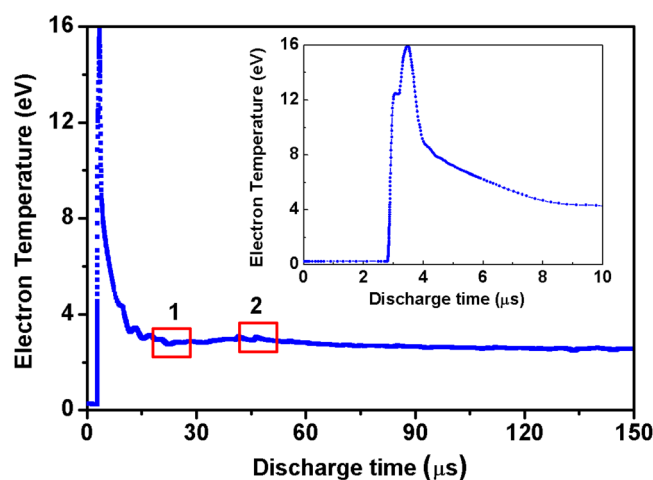
45 μs, decreases, and finally stabilizes to reach the reaction equilibrium for each particle.

To obtain the accurate particle evolution process in the plasma and verify the simulation results, a single photon counter SR430 (Stanford Research Systems) is used to enhance the optical signal and achieve high-speed collection on the atomic emission spectrometer SR-500i-B1-R (ANDOR). The time-resolved optical emission spectroscopy (OES) has an ultrahigh time resolution of 400 ns. The light emitted by the plasma goes through a quartz window and is collected by the ME-OPT-0007 (ANDOR) light collector aligned with the central axis of the cylindrical cathode. Figures 6(a) and 6(b) reveal the evolution of the 4 typical particles: N (750.4 nm), Ar^{+} (335.1 nm), Cr (432.0 nm), and Cr^{+} (524.0 nm). To ensure fast data acquisition without losing discharge details, the measurement precision of OES is set to 625 ns. Many inflection points can be found from the spectral evolution curve of each particle. The number and occurrence sequence of the inflection points are basically consistent with the simulation results, although the spectral results are slightly delayed compared with the simulation results mainly because the global model simulates the behavior of
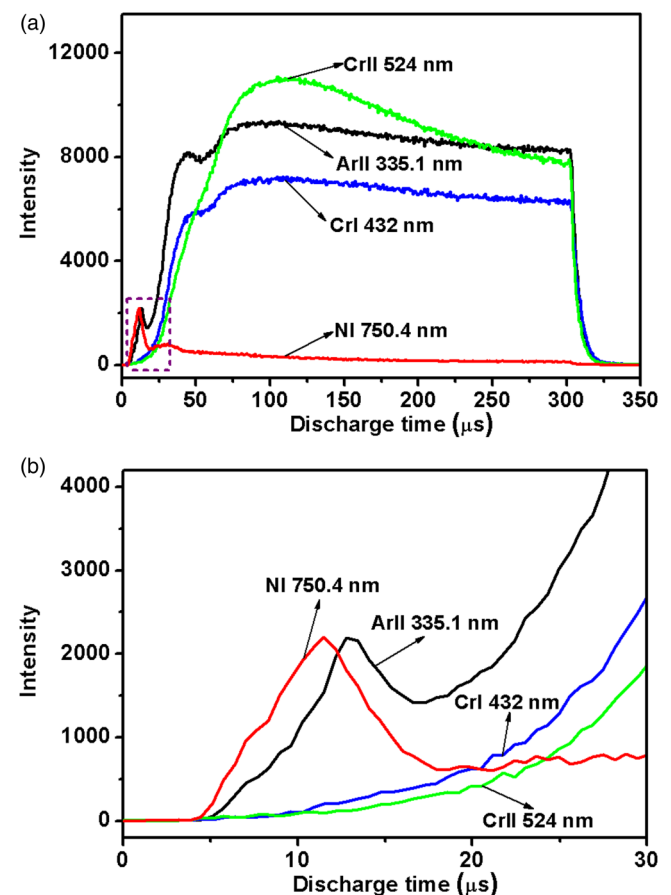

FIG. 5. Electron temperature vs discharge time.

FIG. 6. (a) Spectra of N, Ar^{+}, Cr, and Cr^{+} in a pulse. (b) Spectra of N, Ar^{+}, Cr, and Cr^{+} in the first 30 μs.

particles in the ionization region while the spectrum can only detect the particles in the center of the cylindrical cathode. The spectral intensities of Cr and Cr^+ are similar to those of the simulation, while the Ar^+ intensity obtained after the discharge balance is larger than the simulation. It may be because the measurement position can receive more external argon replenishment and achieve high ionization benefiting from the hollow cathode effect compared with the simulated ionization region. Figure 6(b) depicts the particle spectrum in the first $30\,\mu s$ suggesting that N, Ar^+, Cr, and Cr^+ increase in turn, and the observation is in line with the simulated results in Fig. 3. It should be noted that the significance of the inflections is the alternation of the different physical processes, although they seem a little small, which just means the very fast and unobvious evolution and suggests the necessity of the development of the highly time-resolved spectrometry and the significance of the discoveries here.

IV. CONCLUSIONS

In summary, to examine the details in the HiPIMS discharge process in the Ar/N_2 atmosphere, a cylindrical cathode is used to delay plasma diffusion, and a hollow cathode effect modified time-dependent global model is established to assess the plasma particle behavior in a pulse. The results are verified by data acquired on a nanosecond resolution spectral diagnostic system that offers real-time tracking of particles in the plasma. The occurrence and impact of different physical processes including excitation, ionization, sputtering and diffusion are determined in relation to the discharge time. The results reveal that the gas discharge depends on the reaction energy of particles and the metal discharge depends on the sequence of the physical processes. This work is not only helpful for further understanding of HiPIMS discharge process and mechanism but also for better control of the reactive sputtering and effective prevention of the target poisoning.

APPENDIX: DETAILS OF THE GLOBAL MODEL

The reactions and rate coefficients in $Ar/N2/Cr$ discharge plasma and the corresponding reaction rate coefficients in the equations are shown in Table II. The meaning of the parameters in global model can be found in Table III.

Figure 7 is the detailed schematic diagram of the global model showing the particle balance and corresponding reactions of $Ar/N_2/Cr$ plasma in the ionization region. In the cylindrical

TABLE II. Rate coefficients for $Ar/N_2/Cr$ plasma.

Reaction	Rate coefficient ($m^3\,s^{-1}$)	Threshold (eV)
$e + Ar \rightarrow Ar^+ + 2e$	$k_{iz} = 2.3 \times 10^{-14} T_e^{0.59} \exp(-17.44/T_e)$	$E_{iz} = 15.76\,eV$
$e^H + Ar \rightarrow Ar^+ + 2e$	$k_{iz}^H = 8 \times 10^{-14} T_e^{0.16} \exp(-27.53/T_e)$	$E_{iz} = 15.76\,eV$
$e + Ar \rightarrow Ar^m + e$	$k_{ex} = 2.5 \times 10^{-15} T_e^{0.74} \exp(-11.56/T_e)$	$E_{ex} = 11.56\,eV$
$e^H + Ar \rightarrow Ar^m + e$	$k_{ex}^H = 3.84 \times 10^{-14} T_e^{-0.68} \exp(-22.32/T_e)$	$E_{ex} = 11.56\,eV$
$e + Ar \rightarrow Ar + e$	$k_{el} = 2.336 \times 10^{-14} T_e^{1.609} \times \exp(0.0618(\ln T_e)^2 - 0.1171(\ln T_e)^3)$	
$e + Ar^m \rightarrow Ar + e$	$k_{dex} = 4.3 \times 10^{-16} T_e^{0.74}$	$E_{dex} = -11.56\,eV$
$e + Ar^m \rightarrow Ar^+ + 2e$	$k_{miz} = 6.8 \times 10^{-15} T_e^{0.67} \exp(-4.2/T_e)$	$E_{miz} = 4.2\,eV$
$e^H + Ar^m \rightarrow Ar^+ + 2e$	$k_{miz}^H = 5.7 \times 10^{-13} T_e^{-0.33} \exp(-6.82/T_e)$	$E_{miz} = 4.2\,eV$
$e + N_2 \rightarrow N_2^+ + 2e$	$k_{iz,N_2} = k_{iz,N_2}^H = 1.95 \times 10^{-15} T_e^{1.13} \exp(-14.4/T_e)$	$E_{iz,N_2} = 15.6\,eV$
$e + N_2 \rightarrow N_2^m + e$	$k_{ex,N_2} = k_{ex,N_2}^H = 5.81 \times 10^{-15} \exp(-7.57/T_e)$	$E_{ex,N_2} = 6.17\,eV$
$e + N_2 \rightarrow N_2 + e$	$k_{el,N_2} = 1.04 \times 10^{-13} T_e^{0.43} \exp(-0.206/T_e)$	
$e + N_2 \rightarrow 2N + e$	$k_{diss} = 6.15 \times 10^{-15} T_e^{0.81} \exp(-12.8/T_e)$	$E_{diss} = 9.76\,eV$
$e + N_2^+ \rightarrow 2N$	$k_{diss2} = 1.9 \times 10^{-15} T_e^{-0.30}$	
$e + N_2^m \rightarrow N_2^+ + 2e$	$k_{iz,N_2^m} = k_{iz,N_2^m}^H = 3.39 \times 10^{-13} T_e^{-0.176} \exp(-32.4/T_e)$	$E_{iz,N_2^m} = 9.43\,eV$
$e + N \rightarrow N^+ + 2e$	$k_{N,iz} = 3.84 \times 10^{-15} T_e^{0.92} \exp(-12.1/T_e)$	$E_{iz,N} = 14.54\,eV$
$e + N \rightarrow N + e$	$k_{el,N} = 2.18 \times 10^{-13} T_e^{-0.84} \exp(-0.685/T_e)$	
$N_2 + N^+ \rightarrow N + N_2^+$	$k_{N_2-N^+} = 2.0 \times 10^{-17}$	
$N_2^+ + N \rightarrow N^+ + N_2$	$k_{N_2^+-N} = 1.0 \times 10^{-17}$	
$N_2^m + N \rightarrow N + N_2$	$k_{N_2^m-N} = 4.0 \times 10^{-17}$	$E_{dex,N_2^m} = -6.17\,eV$
$N_2^m + N_2 \rightarrow 2N_2$	$k_{N_2^+-N_2} = 3.5 \times 10^{-18}$	$E_{dex,N_2^m} = -6.17\,eV$
$N_2^m \rightarrow N_2 + h\nu$	$k_{dex,N_2^m} = 2.3 \times 10^{-4}$	$E_{dex,N_2^m} = -6.17\,eV$
$Ar^+ + N_2 \rightarrow Ar + N_2^+$	$k_{Ar^+-N_2} = 1.2 \times 10^{-17}$	
$e + Cr \rightarrow Cr^+ + 2e$	$k_{iz,Cr} = \exp(-E_{iz,Cr}/T_e) \times (T_e/E_{iz,Cr}) \sum_{n=0}^{5} a_n[\log_{10}(T_e/E_{iz,Cr})]^n$	$E_{iz,Cr} = 6.8\,eV$
$e + Cr^+ \rightarrow Cr^{2+} + 2e$	$k_{iz,Cr^+} = \exp(-E_{iz,Cr^+}/T_e) \times (T_e/E_{iz,Cr^+}) \sum_{n=0}^{5} a_n[\log_{10}(T_e/E_{iz,Cr^+})]^n$	$E_{iz,Cr^+} = 15.0\,eV$
$Ar^m + Cr \rightarrow Cr^+ + Ar + e$	Hard sphere	$E_P = 4.76\,eV$
$Ar^+ + Cr \rightarrow Cr^+ + Ar$	Hard sphere	

TABLE III. Parameter table of the global model.

Symbol	Meaning	Unit
B	Average magnetic field at the ionization region boundary	mT
I_D	Experiment discharge current	A
U_D	Experiment discharge voltage	V
P	Pressure	Pa
T	Gas temperature	300 K
F_{coll}	Collision frequency	Hz
R_{IR}	The radius of the ionization region	1.5 cm
R_{source}	The radius of the cylindrical cathode	6 cm
S_T	The contact area of the ionization region with the target	cm^2
S_{IR}	Ionization region superficial area	cm^2
V_{IR}	Ionization region volume	cm^3
k	Reaction coefficient	m^3 s^{-1}
γ	The secondary electron emission coefficient	1
Y	Sputtering yield	1
T_e	Electron temperature	eV
n	Number density	m^{-3}
I_{calc}	Simulated discharge current	A
α	Ionization rate	1
β	Ion return probability	1
σ	Collision cross section	m^2
Γ	Particle flux	1/m^2 s

cathode, the ionization region section can be treated as a semicircle. The contact area with the target S_T (m^2), superficial area S_{IR} (m^2), and volume V_{IR} (m^3) can be calculated by integration as shown in Eq. (A1), in which R_{source} (6 cm) is the radius of the cylindrical cathode and R_{IR} (1.5 cm) is the radius of the ionization region,

$$\begin{cases} S_T = 4\pi R_{source} R_{IR}, \\ S_{IR} = \int_0^{\frac{\pi}{2}} 4\pi R_{IR}(R_{source} - R_{IR}\cos(\theta))d\theta + S_T, \\ V_{IR} = \int_0^{\frac{\pi}{2}} 4\pi(R_{source} - R_{IR}\cos(\theta))R_{IR}^2 \sin^2(\theta)d\theta. \end{cases} \quad (A1)$$

According to the generation and the loss of each particle as shown in Fig. 7, the complete particle densities balance equation can be described as follows.

1. Particle balance equation of atoms and ions

(1) Ar atom

$$\frac{dn_{Ar}}{dt} = -(k_{iz}n_e + k_{iz}^H n_e^H)n_{Ar} - (k_{ex}n_e + k_{ex}^H n_e^H)n_{Ar}$$

$$- \Gamma_{Cr,coll}\frac{m_{Cr}}{m_{Ar}}\frac{n_{Ar}}{n_{gas}}\frac{S_{IR} - S_T}{V_{IR}} + k_{Ar^+ - N_2}n_{Ar^+}n_{N_2} + k_{chexc}n_{Ar^+}n_{Cr}$$

$$+ k_P n_{Ar^m}n_{Cr} + (k_{dex}n_e + k_{dex}^H n_e^H)n_{Ar^m} + \Gamma_{Ar,diff}\frac{S_{IR} - S_T}{V_{IR}}, \quad (A2)$$

where the diffusional Ar flux can be described as $\Gamma_{Ar,diff} = \frac{n_{Ar,0} - n_{Ar}}{4}u_{Ar}$, in which $n_{Ar,0}$ is the Ar density outside

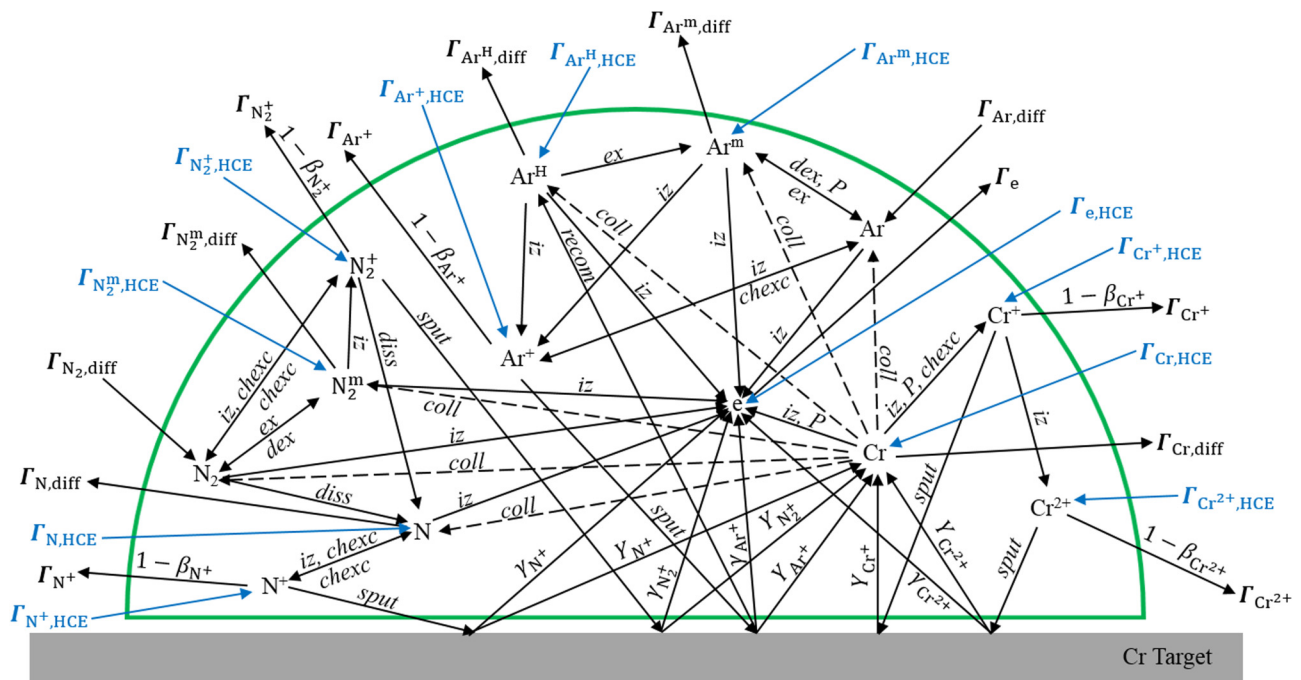**FIG. 7.** Detailed schematic diagram of the global model showing the particle balance and corresponding reactions of Ar/N₂/Cr plasma in the ionization region. The subscripts are defined as follows: diff, diffusion; ex, excitation; Dex, de-excitation; iz, ionization; P, Penning ionization; chexc, charge exchange; coll, collision; recom, recombination; sput, sputtering; and HCE, hollow cathode effect.

ionization region and $u_{\mathrm{Ar}} = \sqrt{\frac{8k_{\mathrm{B}}T}{\pi m_{\mathrm{Ar}}}}$ is the average velocity of Ar at $T = 300$ K. $\boldsymbol{\Gamma}_{\mathrm{Cr,coll}}$ (1/m^2 s) stands for the collision part of the Cr, Cr$^+$, and Cr^{2+} sputtering wind and can be calculated by Eq. (A3),

$$
\begin{cases}
\boldsymbol{\Gamma}_{\mathrm{Cr,coll}} = (\boldsymbol{\Gamma}_{\mathrm{Cr,sput}} + \boldsymbol{\Gamma}_{\mathrm{Cr^+,sput}} + \boldsymbol{\Gamma}_{\mathrm{Cr^{2+},sput}})F_{\mathrm{coll}}, \\
\boldsymbol{\Gamma}_{\mathrm{M,sput}} = \dfrac{n_{\mathrm{M}} u_{T_{\mathrm{Cr}}}}{4}, \quad \mathrm{M = Cr, Cr^+, and\ Cr^{2+}}, \\
u_{T_{\mathrm{Cr}}} = (3k_{\mathrm{B}}T/m_{\mathrm{Cr}})^{1/2}, \\
F_{\mathrm{coll}} = 1 - \exp(-R_{\mathrm{IR}}(\sigma_{\mathrm{Ar\text{-}Cr}}(n_{\mathrm{Ar}} + n_{\mathrm{Ar^m}} + n_{\mathrm{Ar^H}}) + \sigma_{\mathrm{Ar\text{-}N_2}}(n_{\mathrm{N_2}} + n_{\mathrm{N_2^m}}) + \sigma_{\mathrm{Ar\text{-}N}} n_{\mathrm{N}})),
\end{cases}
\tag{A3}
$$

where F_{coll} (Hz) is the collision probability of Cr particles with gas particles in the ionization region, $u_{T_{\mathrm{Cr}}}$ (m/s) is the root mean square velocity, and σ (m^2) is the cross section of collision based on the hard sphere model.

(2) Ar$^+$ ion

$$
\begin{aligned}
\frac{dn_{\mathrm{Ar^+}}}{dt} = {}& -k_{\mathrm{Ar^+\!-N_2}} n_{\mathrm{Ar^+}} n_{\mathrm{N_2}} - k_{\mathrm{chexc}} n_{\mathrm{Ar^+}} n_{\mathrm{Cr}} - \boldsymbol{\Gamma}_{\mathrm{Ar^+}} \frac{S_{\mathrm{T}}}{V_{\mathrm{IR}}} - \boldsymbol{\Gamma}_{\mathrm{Ar^+}} \frac{(S_{\mathrm{IR}} - S_{\mathrm{T}})(1 - \beta_{\mathrm{Ar^+}})}{V_{\mathrm{IR}}} \\
& + (k_{\mathrm{iz}} n_{\mathrm{e}} + k_{\mathrm{iz}}^{\mathrm{H}} n_{\mathrm{e}}^{\mathrm{H}})(n_{\mathrm{Ar}} + n_{\mathrm{Ar^H}}) + (k_{\mathrm{miz}} n_{\mathrm{e}} + k_{\mathrm{miz}}^{\mathrm{H}} n_{\mathrm{e}}^{\mathrm{H}}) n_{\mathrm{Ar^m}} + \boldsymbol{\Gamma}_{\mathrm{Ar^+,HCE}} \frac{(S_{\mathrm{IR}} - S_{\mathrm{T}})}{V_{\mathrm{IR}}}.
\end{aligned}
\tag{A4}
$$

In Eq. (A4), $\boldsymbol{\Gamma}_{\mathrm{Ar^+}} = 0.4 n_{\mathrm{Ar^+}} u_{\mathrm{bohm,Ar^+}}$ is the Ar$^+$ flux leaving the ionization region and $u_{\mathrm{bohm,Ar^+}} = \sqrt{\frac{eT_{\mathrm{e}}}{m_{\mathrm{Ar}}}}$ is the Bohm velocity of the Ar$^+$ ion. The ion return probability can be expressed as Eq. (A5), in which q_{ion} (eV) is the charge number of ion and T_{ion} (eV) is the ion energy,

$$
\beta_{\mathrm{ion}} = \begin{cases}
0, & U_{\mathrm{IR}} \leq T_{\mathrm{ion}}/q_{\mathrm{ion}}, \\
1 - \dfrac{T_{\mathrm{ion}}}{U_{\mathrm{IR}} q_{\mathrm{ion}}}, & U_{\mathrm{IR}} > T_{\mathrm{ion}}/q_{\mathrm{ion}}.
\end{cases}
\tag{A5}
$$

(3) Ar^m metastable atom

$$
\begin{aligned}
\frac{dn_{\mathrm{Ar^m}}}{dt} = {}& -(k_{\mathrm{miz}} n_{\mathrm{e}} + k_{\mathrm{miz}}^{\mathrm{H}} n_{\mathrm{e}}^{\mathrm{H}}) n_{\mathrm{Ar^m}} - k_{\mathrm{P}} n_{\mathrm{Ar^m}} n_{\mathrm{Cr}} - (k_{\mathrm{dex}} n_{\mathrm{e}} + k_{\mathrm{dex}}^{\mathrm{H}} n_{\mathrm{e}}^{\mathrm{H}}) n_{\mathrm{Ar^m}} - \boldsymbol{\Gamma}_{\mathrm{Cr,coll}} \frac{m_{\mathrm{Cr}}}{m_{\mathrm{Ar}}} \frac{n_{\mathrm{Ar^m}}}{n_{\mathrm{gas}}} \frac{S_{\mathrm{IR}} - S_{\mathrm{T}}}{V_{\mathrm{IR}}} - \boldsymbol{\Gamma}_{\mathrm{Ar^m,diff}} \frac{S_{\mathrm{IR}} - S_{\mathrm{T}}}{V_{\mathrm{IR}}} \\
& + (k_{\mathrm{ex}} n_{\mathrm{e}} + k_{\mathrm{ex}}^{\mathrm{H}} n_{\mathrm{e}}^{\mathrm{H}})(n_{\mathrm{Ar}} + n_{\mathrm{Ar^H}}) + \boldsymbol{\Gamma}_{\mathrm{Ar^m,HCE}} \frac{(S_{\mathrm{IR}} - S_{\mathrm{T}})}{V_{\mathrm{IR}}},
\end{aligned}
\tag{A6}
$$

where the flux of Ar^m can be calculated by the equation $\boldsymbol{\Gamma}_{\mathrm{Ar^m,diff}} = \frac{n_{\mathrm{Ar^m}}}{4} u_{\mathrm{Ar}}$.

(4) Ar^H atom

$$
\frac{dn_{\mathrm{Ar^H}}}{dt} = -(k_{\mathrm{iz}} n_{\mathrm{e}} + k_{\mathrm{iz}}^{\mathrm{H}} n_{\mathrm{e^H}}) n_{\mathrm{Ar^H}} - (k_{\mathrm{ex}} n_{\mathrm{e}} + k_{\mathrm{ex}}^{\mathrm{H}} n_{\mathrm{e^H}}) n_{\mathrm{Ar^H}} - \boldsymbol{\Gamma}_{\mathrm{Ar^H,diff}} \frac{S_{\mathrm{IR}} - S_{\mathrm{T}}}{V_{\mathrm{IR}}} - \boldsymbol{\Gamma}_{\mathrm{Cr,coll}} \frac{m_{\mathrm{Cr}}}{m_{\mathrm{Ar}}} \frac{n_{\mathrm{Ar^H}}}{n_{\mathrm{gas}}} \frac{S_{\mathrm{IR}} - S_{\mathrm{T}}}{V_{\mathrm{IR}}} + \boldsymbol{\Gamma}_{\mathrm{Ar^+}} \frac{S_{\mathrm{T}}}{V_{\mathrm{IR}}} + \boldsymbol{\Gamma}_{\mathrm{Ar^H,HCE}} \frac{S_{\mathrm{IR}} - S_{\mathrm{T}}}{V_{\mathrm{IR}}}.
\tag{A7}
$$

(5) N$_2$ molecule

$$
\begin{aligned}
\frac{dn_{\mathrm{N_2}}}{dt} = {}& -(k_{\mathrm{iz,N_2}} n_{\mathrm{e}} + k_{\mathrm{iz,N_2}}^{\mathrm{H}} n_{\mathrm{e}}) n_{\mathrm{N_2}} - (k_{\mathrm{ex,N_2}} n_{\mathrm{e}} + k_{\mathrm{ex,N_2}}^{\mathrm{H}} n_{\mathrm{e}}) n_{\mathrm{N_2}} - k_{\mathrm{diss}} n_{\mathrm{N_2}} n_{\mathrm{e}} - k_{\mathrm{N_2\text{-}N^+}} n_{\mathrm{N_2}} n_{\mathrm{N^+}} - k_{\mathrm{Ar^+\!-N_2}} n_{\mathrm{Ar^+}} n_{\mathrm{N_2}} - \boldsymbol{\Gamma}_{\mathrm{Cr,coll}} \frac{m_{\mathrm{Cr}}}{m_{\mathrm{N_2}}} \frac{n_{\mathrm{Ar^H}}}{n_{\mathrm{gas}}} \frac{S_{\mathrm{IR}} - S_{\mathrm{T}}}{V_{\mathrm{IR}}} \\
& + k_{\mathrm{N_2^+\!-N}} n_{\mathrm{N_2^+}} n_{\mathrm{N}} + k_{\mathrm{N_2^m\text{-}N}} n_{\mathrm{N_2^m}} n_{\mathrm{N}} + k_{\mathrm{N_2^m\text{-}N_2}} n_{\mathrm{N_2^m}} n_{\mathrm{N_2}} + k_{\mathrm{N_2^m\text{-}dex}} n_{\mathrm{N_2^m}} + \boldsymbol{\Gamma}_{\mathrm{N_2,diff}} \frac{S_{\mathrm{IR}} - S_{\mathrm{T}}}{V_{\mathrm{IR}}}.
\end{aligned}
\tag{A8}
$$

(6) N_2^+ atom

$$\frac{dn_{N_2^+}}{dt} = -k_{\text{diss2}}n_{N_2^+}n_e - k_{N_2^+\text{-N}}n_{N_2^+}n_N - \boldsymbol{\Gamma}_{N_2^+}\frac{S_T}{V_{IR}} - \boldsymbol{\Gamma}_{N_2^+}\frac{(S_{IR}-S_T)(1-\beta_{N_2^+})}{V_{IR}} + (k_{\text{iz,N}_2}n_e + k_{\text{iz,N}_2}^H n_e)n_{N_2} + (k_{\text{iz,N}_2^m}n_e + k_{\text{iz,N}_2^m}^H n_e)n_{N_2^m}$$

$$+ k_{N_2\text{-N}^+}n_{N_2}n_{N^+} + k_{\text{Ar}^+\text{-N}_2}n_{\text{Ar}^+}n_{N_2} + \boldsymbol{\Gamma}_{N_2^+,\text{HCE}}\frac{(S_{IR}-S_T)}{V_{IR}}. \tag{A9}$$

(7) N_2^m molecule

$$\frac{dn_{N_2^m}}{dt} = -(k_{\text{iz,N}_2^m}n_e + k_{\text{iz,N}_2^m}^H n_e)n_{N_2^m} - k_{N_2^m\text{-N}}n_{N_2^m}n_N - k_{N_2^m\text{-N}_2}n_{N_2^m}n_{N_2} - k_{\text{dex,N}_2^m}n_{N_2^m} - \boldsymbol{\Gamma}_{N_2^m,\text{diff}}\frac{(S_{IR}-S_T)}{V_{IR}} - \boldsymbol{\Gamma}_{\text{Cr,coll}}\frac{m_{\text{Cr}}}{m_{N_2^m}}\frac{n_{\text{Ar}^H}}{n_{\text{gas}}}\frac{S_{IR}-S_T}{V_{IR}}$$

$$+ (k_{\text{ex,N}_2^m}n_e + k_{\text{ex,N}_2^m}^H n_e)n_{N_2} + \boldsymbol{\Gamma}_{N_2^m,\text{HCE}}\frac{(S_{IR}-S_T)}{V_{IR}}. \tag{A10}$$

(8) N atom

$$\frac{dn_N}{dt} = -(k_{\text{iz,N}}n_e + k_{\text{iz,N}}^H n_e^H)n_N - k_{N_2^+\text{-N}}n_{N_2^+}n_N - \boldsymbol{\Gamma}_{N,\text{diff}}\frac{S_{IR}-S_T}{V_{IR}} - \boldsymbol{\Gamma}_{\text{Cr,coll}}\frac{m_{\text{Cr}}}{m_N}\frac{n_{\text{Ar}^H}}{n_{\text{gas}}}\frac{S_{IR}-S_T}{V_{IR}} + 2k_{\text{diss}}n_{N_2}n_e + 2k_{\text{diss2}}n_{N_2^+}n_e$$

$$+ k_{N_2\text{-N}^+}n_{N_2}n_N + \boldsymbol{\Gamma}_{N,\text{HCE}}\frac{(S_{IR}-S_T)}{V_{IR}} + \boldsymbol{\Gamma}_{N,\text{CrN-sput}}\frac{S_T}{V_{IR}}. \tag{A11}$$

(9) N^+ ion

$$\frac{dn_{N^+}}{dt} = -k_{N_2\text{-N}^+}n_{N^+}n_{N_2} - \boldsymbol{\Gamma}_{N^+}\frac{S_T}{V_{IR}} - \boldsymbol{\Gamma}_{N^+}\frac{(S_{IR}-S_T)(1-\beta_{N^+})}{V_{IR}} + (k_{\text{iz,N}}n_e + k_{\text{iz,N}}^H n_e^H)n_N + k_{N_2^+\text{-N}}n_N n_{N_2^+} + \boldsymbol{\Gamma}_{N^+,\text{HCE}}\frac{(S_{IR}-S_T)}{V_{IR}}. \tag{A12}$$

(10) Cr atom

$$\frac{dn_{\text{Cr}}}{dt} = -(k_{\text{iz,Cr}}n_e + k_{\text{iz,Cr}}^H n_e^H)n_{\text{Cr}} - k_{\text{chexc}}n_{\text{Ar}^+}n_{\text{Cr}} - k_p n_{\text{Ar}^m}n_{\text{Cr}} - \boldsymbol{\Gamma}_{\text{Cr,diff}}\frac{S_{IR}-S_T}{V_{IR}} + \boldsymbol{\Gamma}_{\text{Cr,HCE}}\frac{(S_{IR}-S_T)}{V_{IR}} + \boldsymbol{\Gamma}_{\text{Cr,sput}}\frac{S_T}{V_{IR}}, \tag{A13}$$

where $\boldsymbol{\Gamma}_{\text{Cr,sput}}$ is the sputtering flux of Cr atoms, which can be calculated by Eq. (A14),

$$\boldsymbol{\Gamma}_{\text{Cr,sput}} = (\boldsymbol{\Gamma}_{\text{Ar}^+}Y_{\text{Ar}^+} + \boldsymbol{\Gamma}_{N_2^+}Y_{N_2^+} + \boldsymbol{\Gamma}_{N^+}Y_{N^+} + \boldsymbol{\Gamma}_{\text{Cr}^+}Y_{\text{Cr}^+} + \boldsymbol{\Gamma}_{\text{Cr}^{2+}}Y_{\text{Cr}^{2+}}). \tag{A14}$$

(11) Cr^+ ion

$$\frac{dn_{\text{Cr}^+}}{dt} = -\boldsymbol{\Gamma}_{\text{Cr}^+}\frac{S_T}{V_{IR}} - \boldsymbol{\Gamma}_{\text{Cr}^+}(1-\beta_{\text{Cr}^+})\frac{S_{IR}-S_T}{V_{IR}} + (k_{\text{iz,Cr}^+}n_e + k_{\text{iz,Cr}^+}^H n_e^H)n_{\text{Cr}^+} + (k_{\text{iz,Cr}}n_e + k_{\text{iz,Cr}}^H n_e^H)n_{\text{Cr}}$$

$$+ k_{\text{chexc}}n_{\text{Ar}^+}n_{\text{Cr}} + k_p n_{\text{Ar}^m}n_{\text{Cr}} + \boldsymbol{\Gamma}_{\text{Cr}^+,\text{HCE}}\frac{(S_{IR}-S_T)}{V_{IR}}. \tag{A15}$$

(12) Cr^{2+} ion

$$\frac{dn_{\text{Cr}^{2+}}}{dt} = (k_{\text{iz, Cr}^+}n_e + k_{\text{iz, Cr}^+}^H n_e^H)n_{\text{Cr}^+} - \boldsymbol{\Gamma}_{\text{Cr}^{2+}}\frac{S_T}{V_{IR}} - \boldsymbol{\Gamma}_{\text{Cr}^{2+}}(1-\beta_{\text{Cr}^{2+}})\frac{S_{IR}-S_T}{V_{IR}} + \boldsymbol{\Gamma}_{\text{Cr}^+,\text{HCE}}\frac{(S_{IR}-S_T)}{V_{IR}}. \tag{A16}$$

2. Particle balance equation of electrons

(1) Cold electron

$$\frac{dn_e}{dt} = (k_{\text{iz}}n_e + k_{\text{iz}}^H n_{e^H})(n_{\text{Ar}} + n_{\text{Ar}^H}) + (k_{\text{miz}}n_e + k_{\text{miz}}^H n_{e^H})n_{\text{Ar}^m} + (k_{\text{Criz}}n_e + k_{\text{Criz}}^H n_e^H)n_{\text{Cr}} + (k_{\text{Cr}^+iz}n_e + k_{\text{Cr}^+iz}^H n_e^H)n_{\text{Cr}^+}n_e + (k_{\text{Niz}}n_e + k_{\text{Niz}}^H n_{e^H})n_N$$

$$+ (k_{\text{N}_2\text{iz}}n_e + k_{\text{N}_2\text{iz}}^H n_e)n_{N_2} + (k_{\text{N}_2^m\text{iz}}n_e + k_{\text{N}_2^m\text{iz}}^H n_e)n_{N_2^m} + k_p n_{\text{Cr}}n_{\text{Ar}^m} - \boldsymbol{\Gamma}_e\frac{S_{IR}-S_T}{V_{IR}} + \boldsymbol{\Gamma}_{e,\text{HCE}}\frac{S_{IR}-S_T}{V_{IR}}. \tag{A17}$$

The flux of cold electrons $\boldsymbol{\Gamma}_e$ can be calculated from Eq. (A18),

$$\boldsymbol{\Gamma}_e = D_e \nabla n_{el} + \frac{D_e}{T_e} n_{el} \boldsymbol{E} \approx 0.4 n_e \frac{D_e}{R_{IR}} \left(1 + \frac{U_{IR}}{T_e} \right), \tag{A18}$$

where $n_{el} = 0.4 n_e$ is the electron density on the boundary of the ionization region and $D_e = \frac{1}{\omega \tau} \frac{T_e}{B}$ is the Bohm diffusion coefficient of electrons. The voltage drop U_{IR} in the ionization region can be calculated by the equation $U_{IR} = -\frac{e R_{IR}^2}{\varepsilon_0} (n_{Ar^+} + n_{Cr^+} + 2n_{Cr^{2+}} + n_{N_2^+} + n_{N^+} - n_e - n_{e^H})$.

(2) Hot electron

$$\frac{dn_{e^H}}{dt} = \frac{1}{eU_D/2} \left(\frac{(U_D - U_{IR})I_{se}}{V_{IR}} - Q^H \right), \tag{A19}$$

where $I_{se} = eS_T(\gamma_{Ar^+}\boldsymbol{\Gamma}_{Ar^+} + \gamma_{Cr^+}\boldsymbol{\Gamma}_{Cr^+} + \gamma_{Cr^{2+}}\boldsymbol{\Gamma}_{Cr^{2+}} + \gamma_{N^+}\boldsymbol{\Gamma}_{N^+} + \gamma_{N_2^+}\boldsymbol{\Gamma}_{N_2^+})$ is the secondary electron current and γ is the secondary electron emission coefficient. Q^H (W/m³) stands for the energy loss of hot electrons in the inelastic collision with the atoms, as shown in Eq. (A20),

$$\frac{Q^H}{e} = \sum_j (E_{j,c} + E_{htc})k_{iz,j}^H n_{e^H} n_j - E_{dex}k_{dex}^H n_{e^H} n_{Ar^m},$$
$$j = Ar, Ar^m, N_2, N, Cr, \text{ and } Cr^+, \tag{A20}$$

where $E_{htc} = 10$ eV, representing the energy loss from hot electron to cold electron. $E_{j,c}$ (eV) can be calculated by Eq. (A21),

$$k_{iz,Ar}E_{Ar,c} = k_{iz,Ar}E_{iz,Ar} + k_{ex,Ar}E_{ex,Ar} + k_{el,Ar}\frac{3m_e}{m_{Ar}}T_e,$$

$$k_{iz,Ar^m}E_{Ar^m,c} = k_{iz,Ar^m}E_{iz,Ar^m} + k_{el,Ar^m}\frac{3m_e}{m_{Ar}}T_e,$$

$$k_{iz,N_2}E_{N_2,c} = k_{iz,N_2}E_{iz,N_2} + k_{ex,N_2}E_{ex,N_2} + k_{el,N_2}\frac{3m_e}{m_{N_2}}T_e,$$

$$k_{iz,N}E_{N,c} = k_{iz,N}E_{iz,N} + k_{el,N}\frac{3m_e}{m_N}T_e, \tag{A21}$$

$$k_{iz,Cr}E_{Cr,c} = k_{iz,Cr}E_{iz,Cr} + k_{el,Cr}\frac{3m_e}{m_{Cr}}T_e,$$

$$k_{iz,Cr^+}E_{Cr^+,c} = k_{iz,Cr^+}E_{iz,Cr^+} + k_{el,Cr^+}\frac{3m_e}{m_{Cr^+}}T_e.$$

3. Energy balance equation

$$\frac{d}{dt}\left(\frac{3}{2}en_e T_e \right) = F_{PWR}\frac{P_D}{V_{IR}} - Q - \left(\frac{3}{2}eT_e\boldsymbol{\Gamma}_e\frac{S_{IR} - S_T}{V_{IR}} + \sum_{i=Ar^+,Cr^+,Cr^{2+},N^+,N_2^+} \frac{1}{2}eT_e\boldsymbol{\Gamma}_i\frac{S_T + (S_{IR} - S_T)(1 - \beta_i)}{V_{IR}} \right). \tag{A22}$$

The discharge power $P_D = U_D \times I_D$, which could be directly measured by the discharge experiment. Q (W/m³) stands for the energy variation of collisions between electrons and atoms, as shown in Eq. (A23),

$$\frac{Q}{e} = \sum_j E_{j,c}k_{iz,j}n_e n_j - E_{dex}k_{dex}n_e n_{Ar^m} - E_{N_2^m-N}k_{N_2^m-N}n_{N_2^m}n_N - E_{N_2^m-N_2}k_{N_2^m-N_2}n_{N_2^m}n_{N_2} - E_P k_P n_{Cr}n_{Ar^m}. \tag{A23}$$
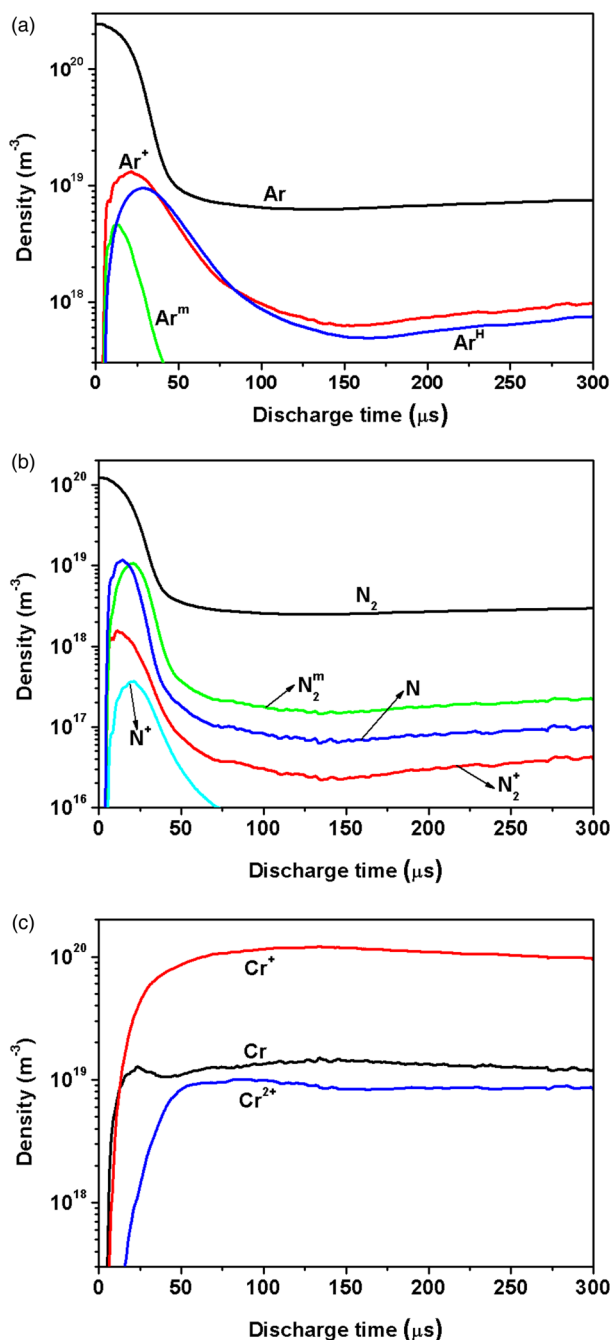
FIG. 8. Density evolution curves with time: (a) Ar, (b) N, and (c) Cr in the whole HiPIMS pulse.

REFERENCES

[1]V. Kouznetsov, K. Macák, J. M. Schneider, U. Helmersson, and I. Petrov, Surf. Coat. Technol. **122**, 290 (1999).

[2]J. Alami, J. T. Gudmundsson, J. Bohlmark, J. Birch, and U. Helmersson, Plasma Sources Sci. Technol. **14**, 525 (2005).

[3]J. T. Gudmundsson, P. Sigurjonsson, P. Larsson, D. Lundin, and U. Helmersson, J. Appl. Phys. **105**, 123302 (2009).

[4]J. Bohlmark, J. Alami, C. Christou, and A. P. Ehiasarian, and U. Helmersson. J. Vac. Sci. Technol. A **23**, 18 (2005).

[5]E. Oks and A. Anders, J. Appl. Phys. **105**, 093304 (2009).

[6]D. Lundin, P. Larsson, E. Wallin, M. Lattemann, N. Brenning, and U. Helmersson, Plasma Sources Sci. Technol. **17**, 035021 (2008).

[7]A. Anders, Surf. Coat. Technol. **205**, S1 (2011).

[8]A. P. Ehiasarian, J. G. Wen, and I. Petrov, J. Appl. Phys. **101**, 054301 (2007).

[9]A. P. Ehiasarian, P. E. Hovsepian, L. Hultman, and U. Helmersson, Thin Solid Films **457**, 270 (2004).

[10]J. Alami, K. Sarakinos, F. Uslu, and M. Wuttig, J. Phys. D Appl. Phys. **42**, 015304 (2009).

[11]J. Alami, P. O. A. Persson, D. Music, J. T. Gudmundsson, J. Bohmark, and U. Helmersson, J. Vac. Sci. Technol. A **23**, 278 (2005).

[12]A. Anders, J. Andersson, and A. Ehiasarian, J. Appl. Phys. **102**, 113303 (2007).

[13]A. Anders, J. Capek, M. Hala, and L. Martinu. J. Phys. D **45**, 012003 (2012).

[14]S. M. Rossnagel and H. R. Kaufman, J. Vac. Sci. Technol. A **6**, 223 (1988).

[15]D. Horwat and A. Anders, J. Appl. Phys. **108**, 123306 (2010).

[16]B. C. Zheng, Z. Z. Wu, S. H. Cui, S. Xiao, L. L. Liu, H. Lin, R. K. Y. Fu, X. B. Tian, F. Pan, and P. K. Chu, IEEE Trans. Plasma Sci. **47**, 193 (2019).

[17]J. Čapek, M. Hala, O. Zabeida, J. E. Klemberg-Sapieha, and L. Martinu, J. Appl. Phys. **111**, 023301 (2012).

[18]J. Alami, K. Sarakinos, G. Mark, and M. Wuttig, Appl. Phys. Lett. **89**, 154104 (2006).

[19]A. P. Ehiasarian, R. New, W.-D. Munz, L. Hultman, U. Helmersson, and V. Kouznetsov, Vacuum **65**, 147 (2002).

[20]J. Bohlmark, M. Lattemann, J. T. Gudmundsson, A. P. Ehiasarian, Y. A. Gonzalvo, N. Brenning, and U. Helmersson, Thin Solid Films **515**, 1522 (2006).

[21]S. M. Meier, A. Hecimovic, T. V. Tsankov, D. Luggenhölscher, and U. Czarnetzki, Plasma Sources Sci. Technol. **27**, 035006 (2018).

[22]S. Tsikata, B. Vincent, T. Minea, A. Revel, and C. Ballage, Plasma Sources Sci. Technol. **28**, 03LT02 (2019).

[23]M. A. Lieberman and R. A. Gottscho, Phys. Thin Films **18**, 1 (1994).

[24]C. Lee and M. A. Lieberman, J. Vac. Sci. Technol. A **13**, 368 (1995).

[25]S. Kim, M. A. Lieberman, A. J. Lichtenberg, and J. T. Gudmundsson, J. Vac. Sci. Technol. A **24**, 2025 (2006).

[26]J. T. Gudmundsson, J. Phys. Conf. Ser. **100**, 082013 (2008).

[27]M. Samuelsson, D. Lundin, J. Jensen, M. Raadu, J. T. Gudmundsson, and U. Helmersson, Surf. Coat. Technol. **205**, 591 (2010).

[28]B. C. Zheng, Z. L. Wu, B. Wu, Y. G. Li, and M. K. Lei, J. Appl. Phys. **121**, 171901 (2017).

[29]M. Hala, N. Viau, O. Zabeida, J. E. Klemberg-Sapieha, and L. Martinu, J. Appl. Phys. **107**, 043305 (2010).

[30]S. H. Cui, Z. Z. Wu, H. Lin, S. Xiao, B. C. Zheng, L. L. Liu, X. K. An, R. K. Y. Fu, X. B. Tian, W. C. Tan, and P. K. Chu, J. Appl. Phys. **125**, 063302 (2019).

[31]Z. H. Wang and S. A. Cohen, J. Vac. Sci. Technol. A **17**, 77 (1999).

[32]S. Xiao, Z. Z. Wu, S. H. Cui, L. L. Liu, B. C. Zheng, H. Lin, R. K. Y. Fu, X. B. Tian, F. Pan, and P. K. Chu, Acta Phys. Sin. **65**, 185202 (2016).

[33]S. H. Cui, Z. Z. Wu, S. Xiao, L. L. Liu, B. C. Zheng, H. Lin, R. K. Y. Fu, X. B. Tian, P. K. Chu, W. C. Tan, and F. Pan, Acta Phys. Sin. **66**, 095203 (2017).

[34]B. C. Zheng, D. Meng, H. L. Che, and M. K. Lei, J. Appl. Phys. **117**, 203302 (2015).

[35]M. A. Raadu, I. Axnas, J. T. Gudmundsson, C. Huo, and N. Brenning, Plasma Sources Sci. Technol. **20**, 065007 (2011).

[36]K. Tao, D. Mao, and J. Hopwood, J. Appl. Phys. **91**, 4040 (2002).

[37]R. S. Freund, R. C. Wetzel, and R. J. Shul, Phys. Rev. A **41**, 5861 (1990).

[38]P. C. Cosby, J. Chem. Phys. **98**, 9544 (1993).

[39]E. G. Thorsteinsson and J. T. Gudmundsson, Plasma Sources Sci. Technol. **18**, 045001 (2009).

[40]M. A. Lennon, K. L. Bell, H. B. Gilbody, J. G. Hughes, A. E. Kingston, M. J. Murray, and F. J. Smith, J. Phys. Chem. Ref. Data **17**, 1285 (1988).

[41]J. F. Ziegler, M. D. Ziegler, and J. P. Biersack, Nucl. Instrum. Methods B **268**, 1818 (2010).

[42]M. A. Lieberman and A. J. Lichtenberg, *Principles of Plasma Discharges and Materials Processing* (John Wiley and Sons Inc., 2005).

[43]A. Anders, Appl. Phys. Lett. **92**, 201501 (2008).